JOURNAL OF PROPULSION AND POWER
Vol. 27, No. 3, May–June 2011

Modeling Neutral Densities Downstream of a Gridded Ion Thruster

George C. Soulas*
NASA John H. Glenn Research Center at Lewis Field, Cleveland, Ohio 43135

DOI: 10.2514/1.B34094

The details of a model for determining the neutral density downstream of a gridded ion thruster are presented. An investigation of the sources of neutrals emanating from the NASA Evolutionary Xenon Thruster ion thruster determined that the most significant contributors to the downstream neutral density include discharge chamber neutrals escaping through the perforated grids, neutrals escaping from the neutralizer, and vacuum facility background neutrals. For the neutral flux through the grids, near- and far-field equations are presented for rigorously determining the neutral density downstream of a cylindrical aperture. These equations are integrated into a spherically-domed convex grid geometry with a hexagonal array of apertures for determining neutral densities downstream of the ion thruster grids. The neutrals escaping from an off-center neutralizer are also modeled assuming diffuse neutral emission from the neutralizer keeper orifice. Finally, the effect of the surrounding vacuum facility neutrals is included and assumed to be constant. The model is used to predict the neutral density downstream of the NASA Evolutionary Xenon Thruster ion thruster with and without neutralizer flow and a vacuum facility background pressure. The impacts of past simplifying assumptions for predicting downstream neutral densities are also examined for the NASA Evolutionary Xenon Thruster ion thruster.

Nomenclature

A	=	particle emission area
c	=	neutral mean thermal speed
$D(\gamma, \beta)$	=	normalized neutral density distribution upstream of the thruster grids
e	=	charge of an electron, 1.602×10^{-19} C
F_{oa}	=	accelerator grid open area fraction
F_{scrn}	=	neutral density correction factor to account for the screen grid, 0.93 for the NASA Evolutionary Xenon Thruster grids
$f(v)$	=	Maxwell–Boltzmann speed distribution function
J_b	=	thruster beam current
J^{++}/J^{+}	=	discharge chamber total doubly-to-singly-charged ion current ratio
K_c	=	neutral transmission probability through an accelerator grid aperture
k	=	hexagon side number
k_B	=	Boltzmann's constant, 1.380×10^{-23} J/K
L	=	length between the surface normal of dA to the downstream neutral density location
l_{cc}	=	grid aperture center-to-center spacing
m	=	number of apertures along the side of a hexagonal array of holes
$\dot{m}_d$	=	total discharge chamber flow rate
m_n	=	neutral gas particle molecular mass
$\dot{m}_{\text{neut}}$	=	neutralizer flow rate
n	=	downstream neutral density
n_{far}	=	far-field equation for the downstream neutral density from an aperture
$n_{\text{far-gridsum}}$	=	far-field equation for the downstream neutral density from a grid by summing individual aperture contributions
$n_{\text{far-gridint}}$	=	far-field equation for the downstream neutral density from a grid by integration of the grid surface
n_{near}	=	downstream neutral density from an aperture in the near field and far field
$n_{\text{near-gridsum}}$	=	downstream neutral density from a grid by summing individual aperture contributions
n_{tank}	=	vacuum facility background neutral density
n_{tot}	=	total downstream neutral density, including contributions from n_{grid}, n_{neut}, and n_{tank}
p	=	number of successive rows defining a hexagonal array of apertures
$p_{\max}$	=	maximum number of rows defining a hexagonal array of apertures
p_{tank}	=	vacuum facility background pressure
R	=	accelerator grid aperture radius
R_{grid}	=	spherically-domed grid radius of curvature
R_{no}	=	neutralizer keeper orifice radius
r	=	radial location
r_{near}	=	radial aperture-to-grid coordinate system transformation
r_{no}	=	neutralizer keeper orifice radial location
T	=	far-field angular distribution function
T_o	=	reservoir or discharge chamber neutral gas temperature
T_{tank}	=	vacuum facility background neutral temperature
t	=	accelerator grid aperture thickness
v	=	neutral particle speed
z	=	axial location
z_{near}	=	axial aperture-to-grid coordinate system transformation
α	=	angle between the dA surface normal and the line connecting the emission and collection sties
β	=	azimuthal angle
Γ	=	neutral flux
γ	=	angle along spherically-domed grid
$\gamma_{\max}$	=	angle along spherically-domed grid to the edge of the perforated grid
δ	=	angle between the downstream surface normal and the line connecting the emission and collection sties
θ	=	neutralizer keeper orifice azimuthal angle
κ	=	aperture wall flux variable
φ	=	cylindrical aperture azimuthal angle
ω	=	solid angle from dA

Presented as Paper 2010-6699 at the 46th AIAA/ASME/SAE/ASEE Joint Propulsion Conference and Exhibit, Nashville, TN, 25–28 July 2010; received 24 August 2010; revision received 11 November 2010; accepted for publication 16 November 2010.

*Electrical Engineer, Propulsion and Propellants Branch, 21000 Brookpark Road, MS 16-1.

Subscripts

f	=	final
grid	=	grid
i	=	initial
neut	=	neutralizer
noff	=	neutralizer keeper emission area offset
o	=	reservoir or discharge chamber
w	=	aperture wall

Superscript

$\bar{}$	=	nondimensionalized value (dimensions are divided by R, densities by n_o, and fluxes by Γ_o)

I. Introduction

THE successful demonstration of NASA's Solar Electric Propulsion Technology Applications Readiness program, or NSTAR, ion thruster on the Deep Space 1 mission and its subsequent use on the Dawn spacecraft have demonstrated the utility and reliability of ion thrusters for NASA's deep space missions [1–5]. As a result of these successes, NASA has continued the development of ion propulsion technology by investing in the NASA Evolutionary Xenon Thruster (NEXT), which represents a next-generation ion propulsion system [6]. The objective of the NEXT project is to advance this next-generation ion propulsion technology to NASA technology readiness level 5, with significant progress towards level 6, to support NASA Science Mission Directorate missions [7]. The NEXT program is developing an advanced ion propulsion system, that includes, in part, a high performance, 7 kW ion thruster with a spherically-domed beam extraction grid system with a chord diameter of 36 cm.

Although the NEXT ion thruster exhibits high propellant utilization efficiencies throughout its throttling range, some unionized propellant, or neutrals, will inevitably escape the ion thruster's discharge chamber and neutralizer. Some of these neutrals can undergo charge exchange with the beam ion plume to create slow-moving charge-exchange ions. These charge-exchange ions are subsequently directed by potentials within the ion beam and charge-exchange plasmas back towards the accelerator grid, where they can erode the grid because of their high energies and limit the service life capability of the thruster. Charge-exchange ions can also be directed away from the thrust axis and possibly towards spacecraft surfaces. Although the energies of these ions are low, modeling of the charge-exchange plasma is typically conducted to understand where these charge-exchange ions are directed and to assess their possible impact on the spacecraft. Properly modeling charge-exchange production requires an accurate understanding of the neutral density distribution downstream of an ion thruster.

In addition to charge-exchange plasma effects on the thruster and spacecraft, the neutrals escaping from the thruster can also affect plasma diagnostics' measurements. For example, measurements of the doubly-charged beam ion current relative to the singly-charged current are affected by differences in charge-exchange cross sections [8]. Specifically, the charge-exchange cross section for singly-charged ions is much larger than that of doubly-charged ions [9]. This can lead to exaggerated doubly-to-singly-charged ion current ratios when measured far downstream of the ion thruster and at high background pressures [8]. Properly modeling this charge-exchange effect again requires an accurate understanding of the neutral density distribution downstream of the ion thruster.

Many past studies have modeled the downstream neutral density emanating from an ion thruster. Unfortunately, most studies made simplifying assumptions that limited the utility of their models. These simplifying assumptions ignored the effect of the grid shape and the neutral efflux "beaming" effect of individual apertures of finite thickness, where thicker aperture walls direct more escaping neutrals along the aperture centerline [10,11]. Very early studies either treated the thruster as a point source for far-field analyses or merely assumed that the thruster was a flat surface with neutral particle emission throughout the surface, allowing for a simpler analytical expression to be used [12,13]. A large number of studies modeled the downstream neutral density using an analytical expression that merely assumed a point source for the neutrals upstream of the thruster grids [14–21]. Another study used an analytical expression that assumed that neutrals were emitted from a flat disk diffusely [22]. And yet other analyses used a Monte Carlo particle-in-cell technique to model the neutral efflux from an ion thruster [23–26]. Such a technique has the benefit of including the impacts of charge-exchange on the velocity distribution of the neutral efflux, for example, but computational difficulties with this technique led to simplifications that included computational boundaries that assumed a flat grid without individual apertures. The failure of all aforementioned studies to capture the effect of the grid shape and the beaming effect of individual apertures reduced the accuracy of the modeled results and limited the utility of the models to the far field.

Three studies did include the effect of the grid shape and two studies included neutral efflux from individual apertures [27–29]. Unfortunately, two studies did not accurately model the neutral efflux beaming effect of individual apertures [27,28]. The other study correctly captured this neutral beaming effect [29]. However, all three studies did not present the equations necessary to recreate their models.

In addition to these simplifying assumptions, almost all of the aforementioned studies assumed that neutrals were only emitted through the thruster grids [12–27,29]. So, most of the studies neglected the contribution of the neutral efflux from the thruster's neutralizer, which will later be shown to be significant.

This paper will present the details of a model for determining the neutral density downstream of a gridded ion thruster. The model will include the effects of the grid's spherical shape and the neutral efflux beaming through cylindrical apertures in both the near field and far field. The first section will examine all sources for neutrals emanating from an ion thruster. The following section will present near- and far-field equations for modeling neutral densities emanating from a

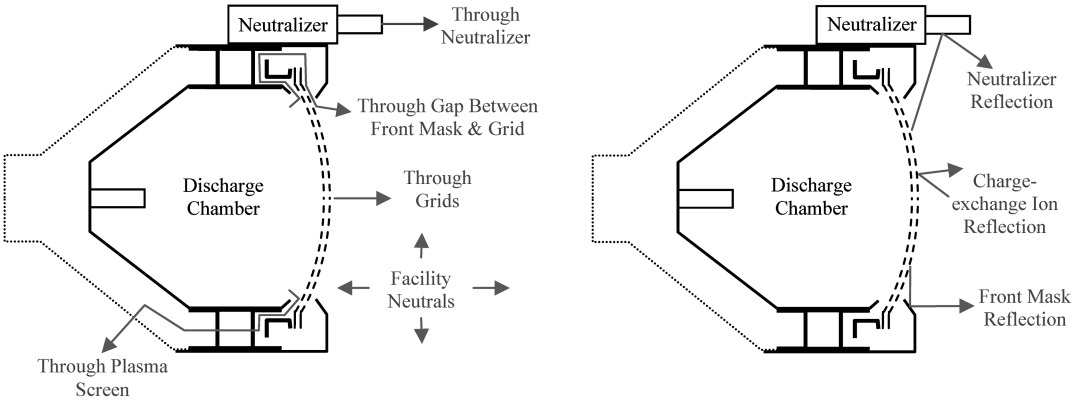

Fig. 1 Unionized propellant escape paths from the thruster (left sketch) and downstream reflections of unionized propellant escaping from through the grids (right sketch).

Table 1 Summary of neutral sources, their relative contributions, and whether they are modeled in this study

Neutral particle source	Relative contribution[a]	Modeled in this study?
Discharge chamber: through grid apertures	99% of discharge chamber neutral loss rate	Yes
Discharge chamber: through gap between front mask and grid	∼0.2% of discharge chamber neutral loss rate	No
Discharge chamber: through plasma screen	∼0.8% of discharge chamber neutral loss rate	No
Neutralizer	40% of discharge chamber neutral loss rate	Yes
Facility background neutrals	6% of discharge chamber neutral density	Yes
Reflected accelerator current	2.7% of discharge chamber neutral loss rate	No
Reflected from neutralizer	<0.2% of discharge chamber neutral loss rate	No
Reflected from front mask	<0.9% of discharge chamber neutral loss rate	No
From charge-exchange with beam ions	Beyond scope of this study	No

[a]Assumes a NEXT ion thruster operating at full power with a background pressure of 6.7×10^{-4} Pa (5×10^{-6} torr).

discharge chamber through cylindrical apertures based on equations derived in other studies [10,11,30]. These equations will then be substituted into the complex perforated grid geometry and this, along with the neutral efflux from the neutralizer, will be used to model neutral densities downstream of an ion thruster. The model will then be used to predict the neutral density downstream of a NEXT ion thruster with and without neutralizer flow and a vacuum facility background pressure. Finally, the impact of past simplifying assumptions for predicting downstream neutral densities will be assessed.

II. Sources of Neutrals from an Ion Thruster

Figure 1 shows sketches of a typical ion thruster with the various sources of neutrals that can emanate from the thruster. As shown in the sketch, neutrals originate as unionized propellant from the discharge chamber and neutralizer, and from the vacuum facility background gas. Neutrals from the discharge chamber can escape through the apertures of the perforated grids, the thruster's plasma screen, and the gap between the front mask and accelerator grid.

Also important are the reflections that neutrals make after they exit the thruster, also shown in Fig. 1. Downstream reflections include neutrals reflected from the front mask and neutralizer, and ions that impact the accelerator grid and leave as neutrals.

Fortunately, two considerations can reduce the complexity of determining downstream neutral densities. The first is related to the low neutral densities within and surrounding the thruster. For a NEXT ion thruster operating at full power, for example, the neutral density within the discharge chamber is estimated to be about 2.5×10^{18} m^{-3}. At this low neutral density, the mean free path for neutral-to-neutral collisions is about 34 cm, which is approximately the NEXT discharge chamber diameter. Within a vacuum facility at a 6.7×10^{-4} Pa (5×10^{-6} torr) background pressure, the mean free path for neutral-to-neutral collisions is greater than 5 m. Such large mean free paths define a rarefied gas flow regime referred to as free molecular flow, where particle-to-particle collisions are so rare that they can be neglected. A benefit of modeling in this regime is that the neutral densities from the various neutral sources can be modeled separately, and the results can be summed to determine a total neutral density. Only within the neutralizer, where pressures can reach as high as about 8900 Pa (67 torr) at full power for the NEXT neutralizer [31], are the mean free paths small enough to be significant. However, these mean free paths increase rapidly as the neutral gas plume expands into vacuum. Because the neutral density downstream of the thruster is ultimately desired, collisional effects within and immediately downstream of the neutralizer cathode can be ignored.

The second consideration that can reduce the complexity of determining downstream neutral densities is the relative contribution of each neutral source. Although neutrals can escape from many regions of an ion thruster, some of the emission and reflection sites can be neglected without significant loss of accuracy. Although there are three escape paths for neutrals to leave the discharge chamber, the vast majority of particles will exit through the grid apertures. This is because the open area between the grids and discharge chamber is only about 11% that of the accelerator grid open area for a NEXT thruster, and because the transmission probability through the grid apertures is much higher. The transmission probabilities through the front mask and plasma screen escape paths were crudely estimated for a NEXT ion thruster [32]. The total amount of propellant leaking through the front mask and plasma screen was estimated to be about 1% of that escaping through the accelerator grid apertures, with most neutrals escaping through the plasma screen. Because this represents such a small percentage of the total leakage, this study will neglect neutrals escaping through the front mask gap and plasma screen.

Neutralizer flow rates are typically large in comparison to the discharge chamber neutral loss rate. Although some of this neutralizer flow will exit the neutralizer as ionized gas, the majority is expected to exit as unionized propellant. Mikellides et al. modeled a NEXT neutralizer during thruster operation at full power [33]. He found that the neutralizer neutral loss rate was 70% of the neutralizer flow during full power operation.[†] Because this represents 40% of the discharge chamber neutral loss rate, the neutral loss from the neutralizer will be modeled in this study.

Vacuum facility background neutrals cannot typically be ignored. Even though vacuum facility pressures can be small (e.g., a 6.7×10^{-4} Pa pressure represents a neutral density that is 6% that of the discharge chamber), it will be shown later that the facility's neutral density contribution is still significant downstream. This is because neutral densities decrease rapidly as they expand into the vacuum chamber. The effect of vacuum facility background neutrals will, therefore, be included in this study.

With regards to neutral reflections, the accelerator current for a NEXT thruster at full power is about 14 mA while the neutral loss rate from the discharge chamber is estimated to be 0.51 equivalent amperes [31]. So, the total flux rate of neutralized accelerator current is only 2.7% of the discharge chamber neutral loss rate. In addition, some of this neutral flux rate will be reflected upstream [32]. Because of this small contribution, ions that impact the accelerator grid and leave as neutrals will also be neglected in this study.

To determine if neutralizer and front mask reflections are significant, the flux of neutrals that escape from the grid apertures and impinge on the neutralizer and front mask was conservatively estimated. It was found that the neutralizer and front mask intercept less than 0.2 and 0.9%, respectively, of the total neutral loss from the discharge chamber. The effect of reflected neutrals from the neutralizer and front mask will, therefore, be neglected in this study.

One other source of neutrals, not shown in Fig. 1, is the fast-moving neutrals created by charge-exchange between downstream neutrals and beam ions. Unfortunately, this requires knowledge of the spatial distribution of beam ion current density, which is beyond the scope of this study. However, the distribution of these neutrals can be determined by later modeling and the result added to that of this study.

Table 1 next summarizes the various neutral escape and reflection sites, their relative contributions, and whether they are modeled in this study. As the table shows, the significant contributors to the downstream neutral density include 1) the neutral flow from the discharge chamber through the grid apertures; 2) neutrals from

[†]Mikellidis, I. G., Private Communication, 11 June 2010.

the neutralizer; and 3) background vacuum facility neutrals. The next section will develop the equations for modeling the downstream neutral density from these neutral sources.

III. Model Development

The following sections will develop the equations necessary to determine the neutral density downstream of an ion thruster. The first section lists the assumptions and fundamental equations used to determine the downstream neutral density. Far- and near-field equations for determining the neutral density downstream of a cylindrical aperture are presented thereafter. The subsequent sections develop the equations for determining downstream neutral density from a spherically-domed convex grid with a hexagonal array of apertures, an off-center neutralizer, and the surrounding vacuum facility neutrals.

A. Assumptions and Fundamental Equations

The equations determined in the following sections are based on the fundamental equations presented within this section. The assumptions used to develop these equations include the following:

1) The neutral density is sufficiently low that free molecular flow conditions exist throughout the modeled domain.

2) Neutrals from a reservoir (e.g., the discharge chamber) have a Maxwell–Boltzmann speed distribution.

3) Equilibrium conditions exist, so that the rate of neutrals leaving the reservoir is equal to the rate of neutrals fed into the reservoir.

4) All wall reflections are diffuse.

5) Neutral adsorption onto the walls and surface diffusion are negligible.

6) Wall temperatures are equal to the neutral particle temperatures.

The geometric relation between a differential element from a neutral particle emission site (i.e., a wall or the upstream reservoir) and the downstream neutral density location is shown in Fig. 2. The variable α is the angle between the neutral emission site surface normal from the differential emitting area, dA_o, to the location of the downstream neutral density, n. The variable L is the distance between the differential emitting area and downstream density.

The downstream neutral density from a reservoir of neutrals can be solved by starting with the Maxwell–Boltzmann phase space speed distribution function [34]. Because equilibrium conditions are assumed, the speed distribution function, $f(v)$, is independent of position (i.e., neutral velocities are isotropic). So, the neutral density downstream of an orifice to a reservoir is

$$n = \iiint_{\infty} n_o \cdot f(v) \cdot \mathrm{d}^3 v = \int_0^{\infty} \int_{\omega_o} f(v) \cdot n_o \cdot \mathrm{d}\omega_o \cdot \mathrm{d}v = \int_0^{\infty} f(v) \cdot \mathrm{d}v \cdot \int_{\omega_o} n_o \cdot \mathrm{d}\omega_o \tag{1}$$

Here, n_o is the neutral density within the reservoir and the differential solid angle, $d\omega_o$, is given by

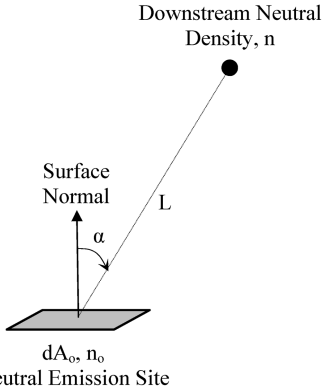

Fig. 2 Geometric relation between a neutral emission site and the downstream neutral density.

$$\mathrm{d}\omega_o = \frac{\mathrm{d}A_o \cdot \cos(\alpha)}{L^2} \tag{2}$$

The first integral in Eq. (1) can be shown to be $1/(4 \cdot \pi)$, so substituting this and Eq. (2) into Eq. (1) yields

$$n = \frac{1}{4 \cdot \pi} \cdot \int_{A_o} n_o \cdot \frac{\cos(\alpha)}{L^2} \cdot \mathrm{d}A_o \tag{3}$$

This equation is in a form that is useful for solving for the downstream neutral density when the emission site is the reservoir. When the emission site is a wall, it is more useful to reexpress Eq. (3) using a particle flux. The resulting equation is given by [32]

$$n = \frac{1}{c \cdot \pi} \cdot \int_{A_w} \Gamma_w(A_w) \cdot \frac{\cos(\alpha)}{L^2} \cdot \mathrm{d}A_w \tag{4}$$

which is in a form that is useful for solving the downstream neutral density when a reflecting wall is the emission site.

B. Neutral Density Downstream of a Single Cylindrical Aperture

The following sections will develop the equations for modeling the neutral density surrounding a grid cylindrical aperture. Two sets of equations will be presented. The first is an expression that was initially derived by Clausing and includes the beaming effect of individual apertures of finite thickness. It is only valid in the far field (i.e., far enough from an aperture to consider it a point source) [10,11]. The second is a series of equations that can be used to rigorously determine neutral density within and downstream of a cylindrical aperture in the near field and far field.

The NEXT ion thruster uses a two grid system for accelerating beam ions. The upstream, or screen, grid is a thin grid with nearly cylindrical apertures and a high open area fraction while the downstream, or accelerator, grid is a thick grid with nearly cylindrical apertures and a much smaller open area fraction. The two cylindrical apertures that a neutral particle has to pass through to escape the discharge chamber present a difficult problem to solve. Fortunately, though, Kuharski et al. modeled a two cylindrical aperture set that had a geometry that was very similar to that of the NEXT thruster [29]. They found that the angular distribution of particles exiting the accelerator grid was well modeled by assuming a single accelerator grid cylindrical aperture and assuming that the upstream neutral

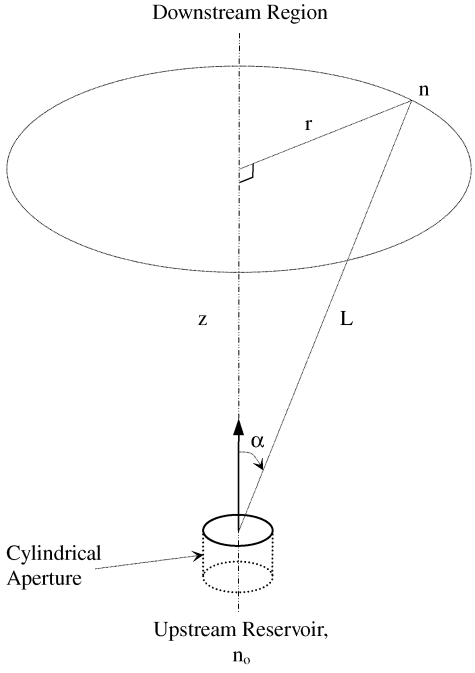

Fig. 3 Far-field neutral density geometry.

density was merely decreased by $0.93x$ due to the screen grid. This simplification was possible because of the large screen aperture diameter and low thickness relative to that of the accelerator grid. This same simplifying assumption will be exploited in this study.

1. Far-Field Equation

Clausing was the first to develop a far-field expression for the angular distribution of particles downstream of a cylindrical aperture [10]. His equation assumes that the aperture is a point source and that the flux of particles from the walls of the aperture is linear as a function of axial thickness, which is an accurate assumption over a range of aperture thickness-to-radius ratios that span from 0 to about 8 [30]. The angular distribution of particles downstream of a cylindrical aperture, $T(\alpha)$, in the far field is given by [10,11]

$$T(\alpha) = \begin{cases} 1 - \left\{ \frac{2}{\pi} \cdot (1-\kappa) \cdot \left[\arcsin\left(\frac{\bar{t}\cdot\tan(\alpha)}{2} \right) + \frac{\bar{t}\cdot\tan(\alpha)}{2} \cdot \sqrt{1 - \left(\frac{\bar{t}\cdot\tan(\alpha)}{2} \right)^2} \right] \right\} + \frac{4}{3\cdot\pi} \cdot (1 - 2\cdot\kappa) \cdot \frac{1 - \left[1 - \left(\frac{\bar{t}\cdot\tan(\alpha)}{2} \right)^2 \right]^{\frac{3}{2}}}{\frac{\bar{t}\cdot\tan(\alpha)}{2}} & \text{if } \alpha \le \arctan\left(\frac{2}{\bar{t}}\right) \\ \text{and} \\ \kappa + \frac{4}{3\cdot\pi} \cdot \frac{1-2\cdot\kappa}{\frac{\bar{t}\cdot\tan(\alpha)}{2}} & \text{if } \alpha > \arctan\left(\frac{2}{\bar{t}}\right) \end{cases} \tag{5}$$

where

$$\kappa = \frac{\sqrt{\bar{t}^2+4} - \bar{t}}{2 + \frac{4}{\sqrt{\bar{t}^2+4}}} \tag{6}$$

Here, t is the accelerator aperture thickness and the bar symbol denotes nondimensionalizing by dividing the thickness with the accelerator aperture radius, R.

Figure 3 next shows the geometry for a single aperture that is treated as a point source. Equation (5) can be used in Eq. (3) to determine the downstream neutral density from a cylindrical aperture in the far field. Note that all variables are independent of dA_o because a point source is assumed, so that integral reduces to $\pi \cdot R^2$. It can be shown that the far-field neutral density, n_{far}, is given in non-dimensional form by

$$\bar{n}_{\text{far}}(\bar{r},\bar{z}) = F_{\text{scrn}} \cdot \frac{1}{4} \cdot T\left[\arccos\left(\frac{\bar{z}}{\sqrt{\bar{r}^2+\bar{z}^2}} \right) \right] \cdot \frac{\bar{z}}{(\bar{r}^2+\bar{z}^2)^{\frac{3}{2}}} \tag{7}$$

Here, neutral density is nondimensionalized with the upstream neutral density, n_o, and r and z are nondimensionalized with the accelerator aperture radius, R. Also, F_{scrn} represents the correction factor to account for the upstream screen grid, which is 0.93 for the NEXT grids as discussed earlier.

2. Near- and Far-Field Equations

Soulas developed equations for rigorously determining neutral density distribution surrounding a cylindrical aperture in the free molecular flow regime [30]. This section will briefly review the development of these equations.

The neutral density downstream of a cylindrical aperture is made up of two components: particles that have a direct line of sight to a downstream location from the reservoir and from the aperture cylindrical walls. In nondimensional form, the downstream neutral density, n_{near}, is given by

$$\begin{aligned} \bar{n}_{\text{near}}(\bar{r},\bar{z}) = \frac{F_{\text{scrn}}}{4\cdot\pi} \cdot \Bigg\{ & \int_{\bar{r}_{oi}}^{\bar{r}_{of}} \int_{\varphi_i}^{\varphi_f} \frac{\bar{z}\cdot\bar{r}_o}{[\bar{z}^2+\bar{r}^2+\bar{r}_o^2-2\cdot\bar{r}\cdot\bar{r}_o\cdot\cos(\varphi)]^{\frac{3}{2}}} \\ & \cdot d\varphi \cdot d\bar{r}_o + \int_{\bar{z}_{wi}}^{\bar{z}_{wf}} \int_{\varphi_i}^{\varphi_f} \frac{\bar{\Gamma}_w(\bar{z}_w)\cdot(1-\bar{r}\cdot\cos(\varphi))}{[(\bar{z}-\bar{z}_w)^2+\bar{r}^2+1-2\cdot\bar{r}\cdot\cos(\varphi)]^{\frac{3}{2}}} \\ & \cdot d\varphi \cdot d\bar{z}_w \Bigg\} \end{aligned} \tag{8}$$

where all dimensions (i.e., r, z, t, r_o, and z_w) are nondimensionalized with the aperture radius, R, and the wall flux, Γ_w, is non-dimensionalized with the reservoir flux, Γ_o. The wall flux was assumed to be linear and its nondimensionalized equation is given by [30]

$$\bar{\Gamma}_w(\bar{z}) = (1-\kappa) + \left(\frac{2\cdot\kappa - 1}{\bar{t}} \right) \cdot \bar{z} \tag{9}$$

The first integral on the right hand side of Eq. (8) represents the contribution of the reservoir to the downstream neutral density while the second integral represents the cylindrical wall's contribution. The

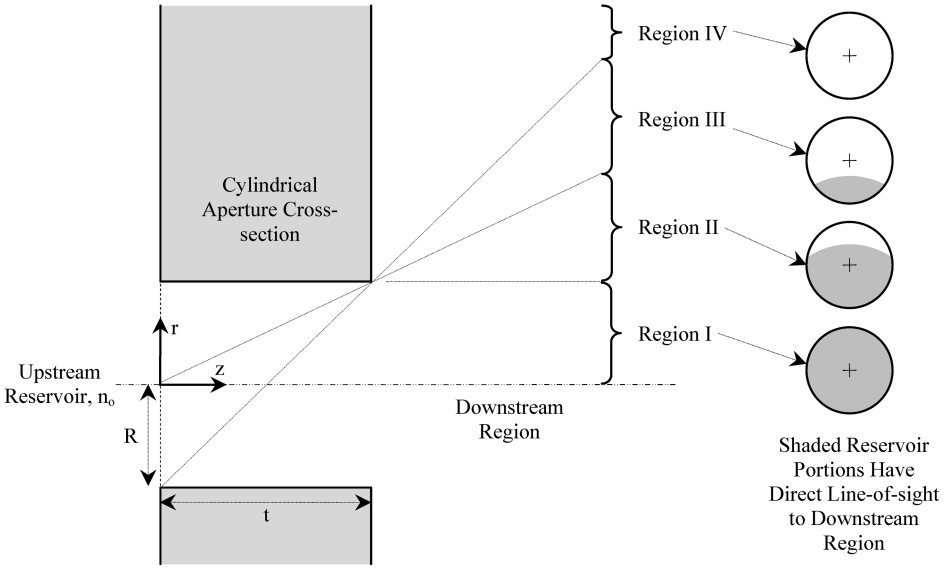

Fig. 4 Definition of downstream regions for the development of the neutral density equations from the upstream reservoir.

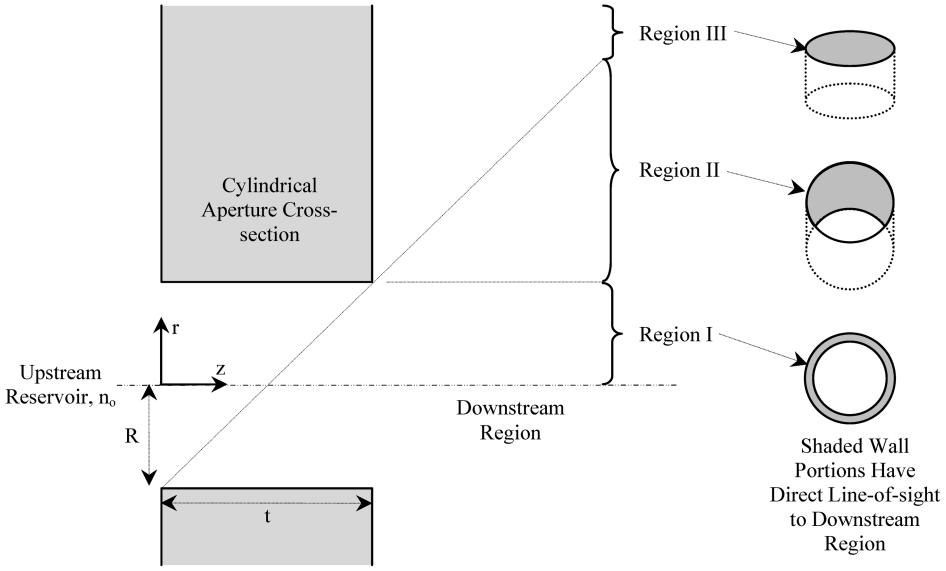

Fig. 5 Definition of downstream regions for the development of the neutral density equations from the cylindrical aperture walls.

limits of integration are a function of the downstream location (i.e., r and z). The contribution of the reservoir and cylindrical wall areas depends on which portion of each area has a direct line of sight to the downstream location. This is illustrated in Figs. 4 and 5. As shown in the figures, all reservoir and cylindrical wall areas have a direct line of sight to downstream locations within region I. But only a portion of the reservoir and cylindrical wall areas have a direct line of sight to downstream locations within regions II and III. And no reservoir particles have a direct line of sight to downstream locations in region IV.

Though complicated, the division of the downstream area into the regions illustrated in Figs. 4 and 5 were used to define a set of equations with different limits of integration that can rigorously determine the neutral density downstream of a cylindrical aperture. The base equation for the downstream density, n_{near}, in nondimensional form is given by

$$\bar{n}_{\text{near}}(\bar{r},\bar{z}) = F_{\text{scrn}} \cdot [\bar{n}_o(\bar{r},\bar{z}) + \bar{n}_w(\bar{r},\bar{z})] \tag{10}$$

convex grid with a hexagonal array of apertures. The first part develops the geometric relation between the downstream neutral density and the grid surface. A cylindrical coordinate system will be used for the downstream neutral density location. The second part applies these equations to determine the downstream neutral density.

Figure 6 shows the geometric relation between the downstream neutral density located at (r, z) in a cylindrical coordinate system and a neutral emission site located on a spherically-domed convex grid with radius of curvature of R_{grid}. The angle between the normal of the neutral emission surface and the desired downstream neutral density location is given by α_{grid} and is separated by distance L_{grid}. The axial distance, z, is defined from the downstream center of the domed grids.

To solve for the downstream neutral density, it is necessary to define α_{grid} and L_{grid} as functions of γ, β, R_{grid}, r, and z. Using the law of cosines, it can be shown that α_{grid} in nondimensional form is given by

$$\alpha_{\text{grid}}(\bar{r},\bar{z},\gamma,\beta) = \arccos\left\{\frac{\left[\frac{\bar{z}+\bar{R}_{\text{grid}}}{\cos(\gamma)} - \bar{R}_{\text{grid}}\right]^2 + \bar{L}_{\text{grid}}^2 - (\bar{z}+\bar{R}_{\text{grid}})^2 \cdot \tan(\gamma)^2 - \bar{r}^2 + 2\cdot(\bar{z}+\bar{R}_{\text{grid}})\cdot\tan(\gamma)\cdot\bar{r}\cdot\cos(\beta)}{2\cdot\left[\frac{\bar{z}+\bar{R}_{\text{grid}}}{\cos(\gamma)} - \bar{R}_{\text{grid}}\right]\cdot\bar{L}_{\text{grid}}}\right\} \tag{11}$$

Using the law of cosines again, the length L_{grid} can be shown to be given in nondimensional form by

$$\bar{L}_{\text{grid}}(\bar{r},\bar{z},\gamma,\beta) = \sqrt{\bar{r}^2 + \bar{R}_{\text{grid}}^2\cdot\sin(\gamma)^2 - 2\cdot\bar{r}\cdot\bar{R}_{\text{grid}}\cdot\sin(\gamma)\cdot\cos(\beta) + \{\bar{z}+\bar{R}_{\text{grid}}\cdot[1-\cos(\gamma)]\}^2} \tag{12}$$

where the equations for the upstream (n_o) and wall (n_w) contributions are given in [32]. Because of the linear wall flux assumption, the double integrals of Eq. (8) could be reduced to single integrals [32]. These equations are applicable to the aperture interior and downstream regions, and that the origin for these equations is the upstream entrance to the cylindrical aperture, as shown in Figs. 4 and 5, unlike the far-field equation.

C. Convex Grid Geometric Equations and Downstream Neutral Density Equations from a Grid

The following section will develop the geometric equations for determining downstream neutral density from a spherically-domed

For both of the preceding equations, all dimensions were nondimensionalized with the accelerator aperture radius, R.

Equations for the locations of individual apertures along the spherically-domed grid are derived in [32] for a hexagonal array of apertures. With these locations and α_{grid} and L_{grid} defined in the preceding equations, the downstream neutral density from a convex spherical dome can now be determined. The far-field neutral density can be solved as was done for Eq. (7). It can be shown that with the far-field angular distribution function, the neutral density downstream of a convex grid, $n_{\text{far-gridsum}}$, is given in nondimensional form by

$$\bar{n}_{\text{far-gridsum}}(\bar{r},\bar{z}) = \frac{F_{\text{scrn}} \cdot T[\alpha_{\text{grid}}(\bar{r},\bar{z},\gamma=0,\beta=0)] \cdot D(\gamma=0,\beta=0)}{4} \cdot \frac{\cos[\alpha_{\text{grid}}(\bar{r},\bar{z},\gamma=0,\beta=0)]}{\bar{L}^2_{\text{grid}}(\bar{r},\bar{z},\gamma=0,\beta=0)}$$
$$+ \sum_{p=1}^{p_{\max}} \sum_{k=1}^{6} \sum_{m=0}^{p-1} \begin{cases} \frac{F_{\text{scrn}} \cdot T[\alpha_{\text{grid}}(\bar{r},\bar{z},\gamma_{m,p},\beta_{k,m,p})] \cdot D(\gamma_{m,p},\beta_{k,m,p})}{4} \cdot \frac{\cos[\alpha_{\text{grid}}(\bar{r},\bar{z},\gamma_{m,p},\beta_{k,m,p})]}{\bar{L}^2_{\text{grid}}(\bar{r},\bar{z},\gamma_{m,p},\beta_{k,m,p})} & \text{if } \gamma_{m,p} \le \gamma_{\max} \\ \text{and} & \\ 0 & \text{if } \gamma_{m,p} > \gamma_{\max} \end{cases} \quad (13)$$

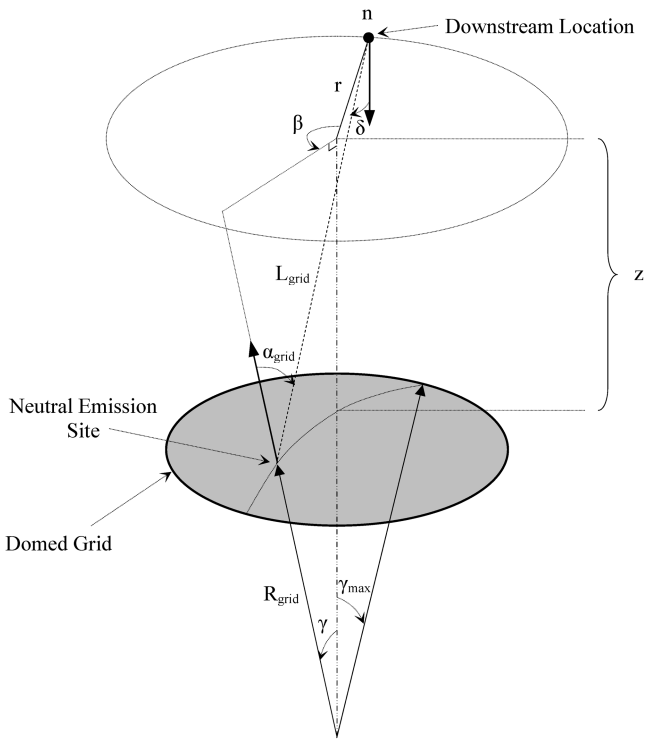

Fig. 6 The geometric relation between the downstream neutral density located at (r, z) and the neutral emission site located on spherically-domed convex grid.

The first term on the right hand side of the preceding equation is the center aperture's contribution while the second term includes the contributions of all other apertures. The second term on the right hand side also includes conditional statements to ensure that apertures located beyond the aperture pattern boundary are not included in the calculation. The variables α_{grid} and L_{grid} are defined in Eqs. (11) and (12), respectively, and γ, β, and $p_{\max}$ are defined in [32]. This equation was generalized by accounting for variations in the upstream neutral density within the discharge chamber as a function of γ and β (i.e., across the grids). It is assumed that upstream neutral density distribution can be described by

$$n_o(\gamma,\beta) = n_o \cdot D(\gamma,\beta) \quad (14)$$

where D is a distribution function and n_o is now an average neutral density. Equation (13) is nondimensionalized with the average discharge chamber upstream neutral density, n_o.

Further away from the grid, it will be shown that it is reasonable to neglect individual apertures and treat the entire grid surface as a neutral-emitting surface. Equations (11), (12), and (14) can be substituted into Eq. (3) to yield the neutral density downstream of a convex grid, $n_{\text{far-gridint}}$, in nondimensional form:

$$\bar{n}_{\text{far-gridint}}(\bar{r},\bar{z}) = \frac{\bar{R}^2_{\text{grid}} \cdot F_{\text{oa}} \cdot F_{\text{scrn}}}{4 \cdot \pi} \cdot \int_0^{2\cdot\pi} \int_0^{\gamma_{\max}} D(\gamma,\beta) \cdot T[\alpha_{\text{grid}}(\bar{r},\bar{z},\gamma,\beta)] \cdot \frac{\cos[\alpha_{\text{grid}}(\bar{r},\bar{z},\gamma,\beta)]}{\bar{L}^2_{\text{grid}}(\bar{r},\bar{z},\gamma,\beta)} \cdot \sin(\gamma) \cdot \mathrm{d}\gamma \cdot \mathrm{d}\beta \quad (15)$$

Here, the equation is nondimensionalized with the average discharge chamber upstream neutral density (n_o), α_{grid}, L_{grid}, and T are given by

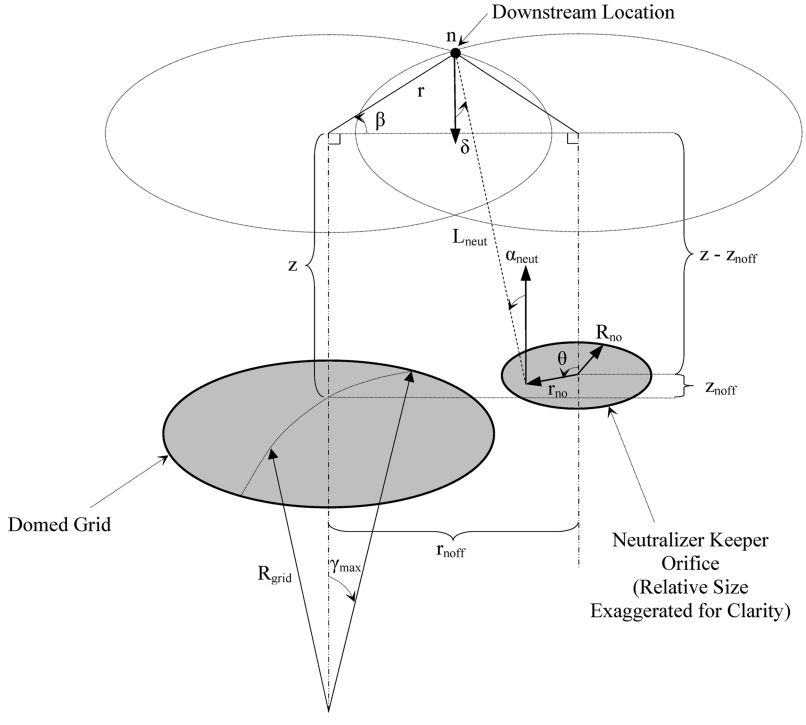

Fig. 7 The geometric relation between the downstream neutral density located at (r, z) and the neutralizer keeper orifice emission area.

Eqs. (11), (12), and (5), respectively, and F_{oa} is the accelerator grid open area fraction, which is defined in [32].

Equation (10), which is valid in the near field and far field, can also be applied to the grids. This is done by transforming r and z of the aperture coordinate system in Eq. (10) to the grid coordinate system (i.e., by defining r and z in the aperture coordinate system as functions of γ, β, R_{grid}, r, and z in the grid coordinate system of Fig. 6). The contribution of all apertures can then be summed in a manner similar to Eq. (13). It can be shown that the result in nondimensional form is

$$\bar{n}_{\text{near-gridsum}}(\bar{r},\bar{z}) = \bar{n}_{\text{near}}[\bar{r}_{\text{near}}(\bar{r},\bar{z},\gamma=0,\beta=0),\bar{z}_{\text{near}}(\bar{r},\bar{z},\gamma=0,\beta=0)]\cdot D(\gamma=0,\beta=0) + \sum_{p=1}^{p_{\max}}\sum_{k=1}^{6}\sum_{m=0}^{p-1}\begin{cases}\bar{n}_{\text{near}}[\bar{r}_{\text{near}}(\bar{r},\bar{z},\gamma_{m,p},\beta_{k,m,p}),\bar{z}_{\text{near}}(\bar{r},\bar{z},\gamma_{m,p},\beta_{k,m,p})]\cdot D(\gamma_{m,p},\beta_{k,m,p}) & \text{if } \gamma_{m,p}\le\gamma_{\max}\\ \text{and} & \\ 0 & \text{if } \gamma_{m,p}>\gamma_{\max}\end{cases} \tag{16}$$

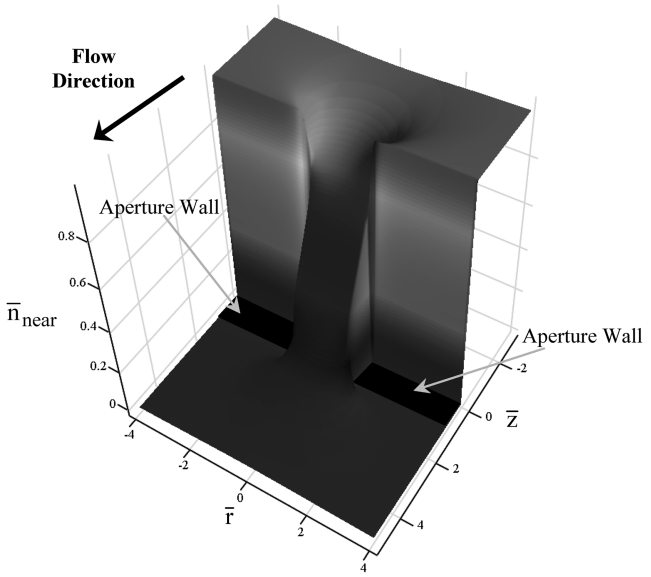

Fig. 8 Neutral density surrounding a single NEXT accelerator aperture.

where n_{near} is given in Eq. (10), γ, β, and $p_{\max}$, are given in [32], D is given by Eq. (14), and

$$\bar{r}_{\text{near}} = \bar{L}_{\text{grid}}(\bar{r},\bar{z},\gamma,\beta)\cdot\sin[\alpha_{\text{grid}}(\bar{r},\bar{z},\gamma,\beta)] \tag{17}$$

and

$$\bar{z}_{\text{near}} = \bar{L}_{\text{grid}}(\bar{r},\bar{z},\gamma,\beta)\cdot\cos[\alpha_{\text{grid}}(\bar{r},\bar{z},\gamma,\beta)] + \bar{t} \tag{18}$$

The variables α_{grid} and L_{grid} are given by Eqs. (11) and (12), respectively. Equation (16) is nondimensionalized with the average discharge chamber neutral density, n_o.

D. Neutralizer Downstream Neutral Density

For the neutralizer, the gas upstream of the cathode orifice is collisional, so Eqs. (5) and (8) cannot be applied. Unfortunately, accurately modeling the gas expansion process through the cathode orifice is beyond the scope of this study. However, because the neutralizer discharge would likely randomize the spatial velocity distribution of the neutral gas that escapes the cathode, this study will assume that neutrals exit the neutralizer keeper orifice diffusely.

Figure 7 shows the geometric relation between the downstream neutral density located at (r, z) in a cylindrical coordinate system and

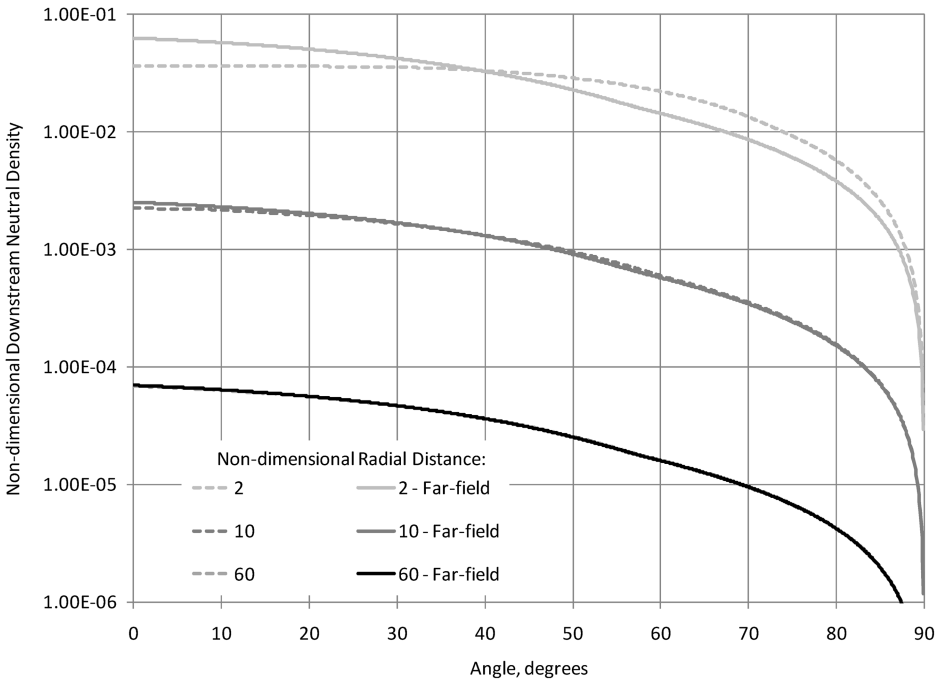

Fig. 9 Nondimensional neutral density angular distributions for a variety of radial distances in a spherical coordinate system that is centered at the downstream aperture center for a NEXT accelerator aperture. Solid lines were determined from Eq. (10) and dashed lines from Eq. (7).

the neutralizer keeper orifice. The angle between the normal of the neutralizer keeper orifice emission area and the downstream neutral density is given by α_{neut} and is separated by distance L_{neut}. The angle β is defined as being 0° through the neutralizer centerline. The variables z_{noff} and r_{noff} are the axial and radial offsets, respectively, of the neutralizer keeper orifice emission area center from the downstream center of the domed grid. The variables r_{no} and θ are the radius and azimuthal angle for the neutralizer keeper orifice area, respectively.

To solve for the downstream neutral density, it is necessary to define α_{neut} and L_{neut} as functions of $r, z, \beta, r_{\text{no}}$, and θ. It can be shown that α_{neut} is given in nondimensional form by

$$\alpha_{\text{neut}}(\bar{r}, \bar{z}, \beta, \bar{r}_{\text{no}}, \theta) = \arccos\left\{\frac{\bar{z} - \bar{z}_{\text{noff}}}{\bar{L}_{\text{neut}}(\bar{r}, \bar{z}, \beta, \bar{r}_{\text{no}}, \theta)}\right\} \tag{19}$$

The length L_{neut} can be shown to be given in nondimensional form by

$$\bar{L}_{\text{neut}}(\bar{r}, \bar{z}, \beta, \bar{r}_{\text{no}}, \theta) = \sqrt{\bar{r}_{\text{noff}}^2 + \bar{r}^2 - 2 \cdot \bar{r}_{\text{noff}} \cdot \bar{r} \cdot \cos(\beta) + \bar{r}_{\text{no}}^2 - 2 \cdot \sqrt{\bar{r}_{\text{noff}}^2 + \bar{r}^2 - 2 \cdot \bar{r}_{\text{noff}} \cdot \bar{r} \cdot \cos(\beta)} \cdot \bar{r}_{\text{no}} \cdot \cos(\theta) + (\bar{z} - \bar{z}_{\text{noff}})^2} \tag{20}$$

For both of the aforementioned equations, all dimensions were nondimensionalized with the accelerator aperture radius, R.

With α_{neut} and L_{neut} defined in the preceding equations, the downstream neutral density from the neutralizer can now be determined. The neutral density within the keeper orifice can be solved as was done for Eq. (7). It can be shown that the neutral density downstream of a neutralizer, n_{neut}, is given in nondimensional form by [32]

$$\bar{n}_{\text{neut}}(\bar{r}, \bar{z}, \beta) = \begin{cases} \frac{\dot{m}_{\text{neut}}}{m_n \cdot c \cdot \pi^2 \cdot R_{\text{no}}^2 \cdot n_o} \cdot \int_0^{2\cdot\pi} \int_0^{\bar{R}_{\text{no}}} \frac{\cos[\alpha_{\text{neut}}(\bar{r}, \bar{z}, \beta, \bar{r}_{\text{no}}, \theta)]}{\bar{L}_{\text{neut}}^2(\bar{r}, \bar{z}, \beta, \bar{r}_{\text{no}}, \theta)} \cdot \bar{r}_{\text{no}} \cdot \mathrm{d}\bar{r}_{\text{no}} \cdot \mathrm{d}\theta & \text{if } \bar{z} \geq \bar{z}_{\text{noff}} \\ \text{and} & \\ 0 & \text{if } \bar{z} < \bar{z}_{\text{noff}} \end{cases} \tag{21}$$

Here, $\dot{m}_{\text{neut}}$ is the neutralizer mass flow rate, R_{no} is the neutralizer keeper orifice radius, m_n is the molecular mass of the neutral gas, c is the neutral mean thermal speed, and α_{neut} and L_{neut} are given by Eqs. (19) and (20), respectively. The neutralizer neutral density was nondimensionalized with average discharge chamber upstream neutral density, n_o. The conditionals ensure that neutralizer neutrals do not contribute to the density for axial locations less than z_{noff} because of the lack of a direct line of sight to those locations.

E. Background Vacuum Facility Neutral Density

The background neutrals within the vacuum facility are those particles from the thruster (i.e., neutrals, beam ions, charge-exchange ions, and neutralizer ions) that have been reflected from a facility surface. Although the vacuum facility neutrals will typically have a lower temperature than those neutrals emanating from the thruster (see, for example, [35] for NEXT ion thruster temperatures), it will be assumed that vacuum facility neutrals reflected from thruster surfaces will still have vacuum facility wall temperatures and are reflected diffusely. In addition, the neutral density is assumed to be uniform throughout the vacuum facility, which is reasonable for thruster operation in large vacuum facilities.

Because of the aforementioned assumptions, the inclusion of vacuum facility neutrals is straightforward. The background facility neutral density, n_{tank}, as a function of pressure and wall temperature is given in nondimensional form by

$$\bar{n}_{\text{tank}} = \frac{n_{\text{tank}}}{n_o} = \frac{p_{\text{tank}}}{k_B \cdot T_{\text{tank}} \cdot n_o} \tag{22}$$

Here, p_{tank} and T_{tank} are the vacuum facility background pressure and wall temperature and k_B is the Boltzmann constant.

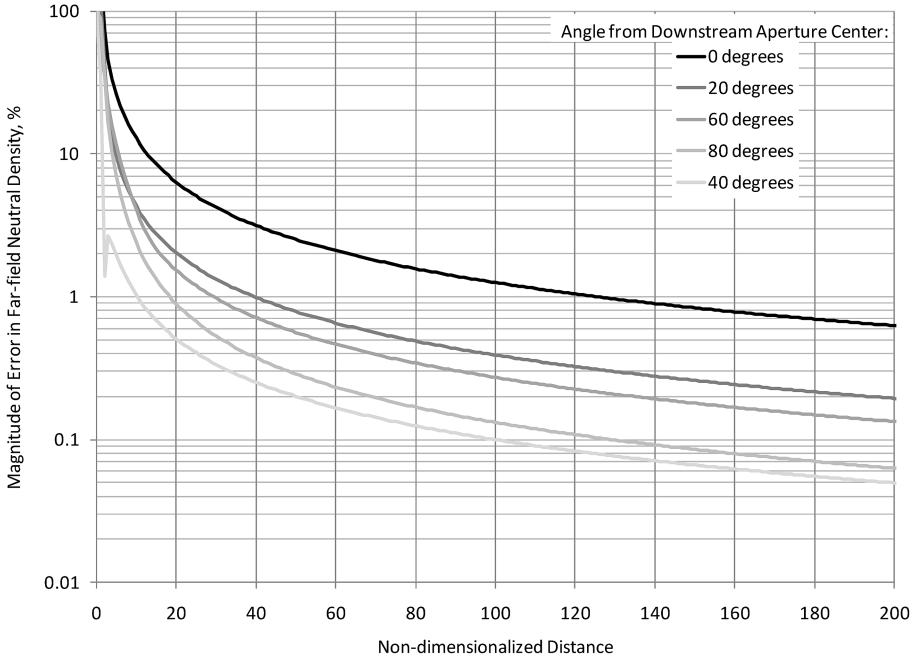

Fig. 10 Far-field neutral density equation error as a function of radial distance at various angles in a spherical coordinate system that is centered at the downstream aperture center for a NEXT accelerator aperture.

F. Total Neutral Density Downstream of an Ion Thruster

The downstream neutral density contributions of each neutral source can be added together to determine the total downstream neutral density. So, the total neutral density downstream of an ion thruster, n_{tot}, is given in nondimensional form by

$$\bar{n}_{\text{tot}}(\bar{r},\bar{z},\beta) = \bar{n}_{\text{grid}}(\bar{r},\bar{z}) + \bar{n}_{\text{neut}}(\bar{r},\bar{z},\beta) + \bar{n}_{\text{tank}} \tag{23}$$

Here, n_{grid} is the discharge chamber contribution given by either Eq. (13), Eq. (15), or Eq. (16); n_{neut} is the neutralizer contribution given by Eq. (21); and n_{tank} is the vacuum facility contribution given by Eq. (22). Note that only the neutralizer density is a function of β, which is 0° in the direction of the neutralizer. Although the hexagonal pattern of the apertures within the grid leads to a dependence on β for Eqs. (13) and (16), it is neglected in this equation because the pattern is nearly axisymmetric for the typically small accelerator grid apertures.

All of the terms within Eq. (23) are nondimensionalized with the average discharge chamber neutral density, n_o. It can be shown that this neutral density is given by

$$n_o = \frac{\dot{m}_d - J_b \cdot \frac{m_n}{e} \cdot \frac{1+\frac{1}{2}\frac{J^{++}}{J^+}}{1+\frac{J^{++}}{J^+}}}{\sqrt{2\cdot\pi\cdot k_B \cdot T_o \cdot m_n} \cdot R_{\text{grid}}^2 \cdot [1-\cos(\gamma_{\max})] \cdot F_{\text{oa}} \cdot K_c \cdot F_{\text{scrn}}} \tag{24}$$

Here, $\dot{m}_d$ is the total discharge flow rate, J_b is the beam current, e is the charge of an electron (i.e., 1.602×10^{-19} C), J^{++}/J^+ is the discharge chamber total doubly-to-singly-charged ion current ratio, T_o is the discharge chamber neutral gas temperature, and K_c is the transmission probability of neutrals through an accelerator grid aperture and is defined in [32]. Equation (24) is the neutral loss rate equation of [36] rearranged to solve for neutral density and corrected with the discharge chamber's doubly-to-singly-charged beam current ratio.

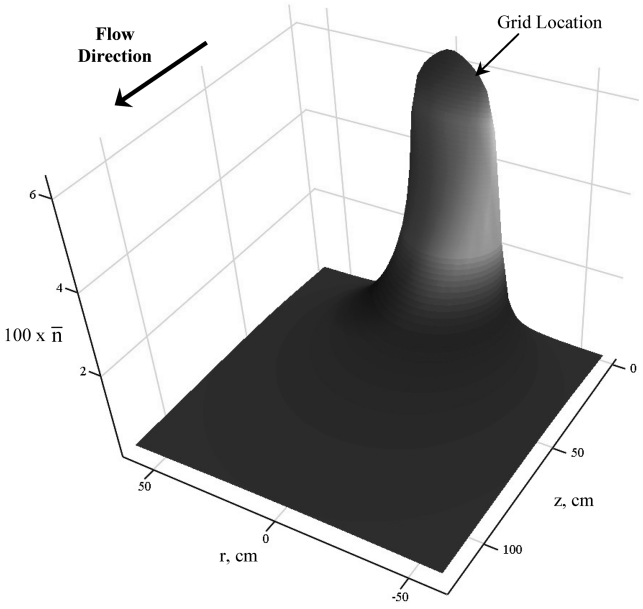

Fig. 11 Nondimensional neutral density downstream of a NEXT ion thruster. The neutral density within the discharge chamber is assumed constant.

IV. Results

The following sections will present the results of the neutral density model developed in this study. Neutral densities from a single aperture and a NEXT grid will be presented, and near- and far-field models will be compared. The neutral density downstream of a NEXT ion thruster will be presented with and without neutralizer flow and a vacuum facility background pressure. Model verification will also be discussed. Finally, the impact of past simplifying assumptions for predicting downstream neutral densities will be assessed.

A. Downstream Neutral Density from a Single Aperture

The neutral density surrounding a single aperture is shown in Fig. 8 for a NEXT accelerator grid cylindrical aperture. The figure was modeled with Eq. (10) for the aperture interior and downstream regions. Figure 8 also includes additional equations derived in [30] for the upstream region. The figure shows a depleted neutral density zone immediately upstream of the aperture, and that the density drops rapidly from the upstream region to the downstream region, through the aperture. The neutral density drops to less than 10% of the upstream value within 1 aperture radius of the downstream surface.

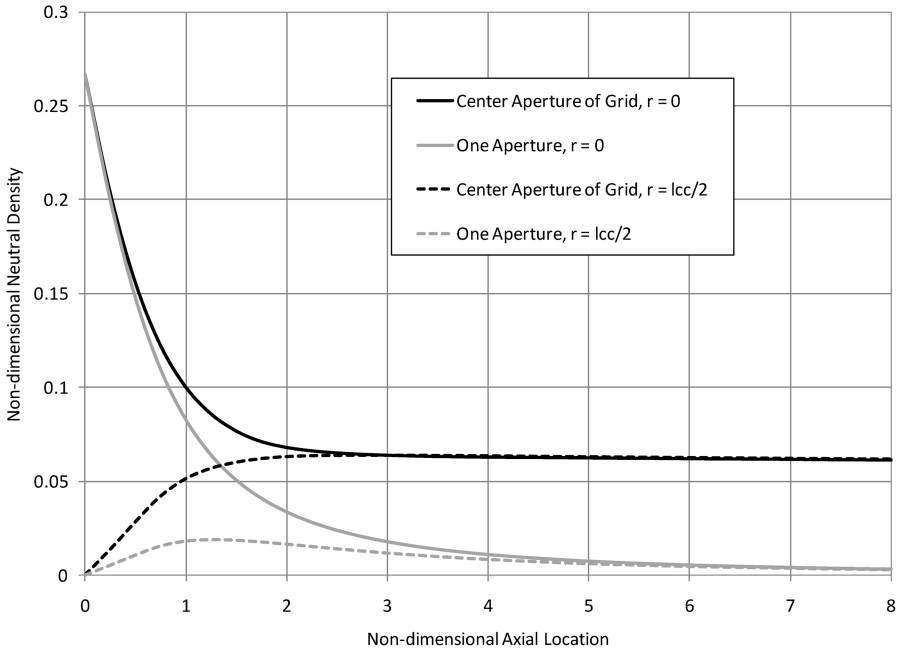

Fig. 12 Nondimensional downstream neutral density from a NEXT ion thruster along the grid centerline and at $r = l_{cc}/2$ comparing the effect of the multiple apertures of a grid to that of a single aperture.

The far-field nondimensional neutral density equation of Eq. (7) is compared with that calculated with the more rigorous Eq. (10) in Fig. 9. Here, the neutral density was determined at fixed radial distances from the downstream center of the aperture from 2 to 60 radii while the angle was varied (i.e., a spherical coordinate system was used) to determine angular distributions. The figure illustrates that at increasing distances from the aperture, the far-field angular distribution becomes equal to that of the Eq. (10) and that the worst-case error in the far-field equation occurs along the axial centerline of the aperture.

The error in the far-field equation of Eq. (7) is plotted in Fig. 10 as a function of nondimensional radial distance from the downstream aperture center at various angles for a NEXT accelerator grid aperture. The figure shows that maximum far-field equation errors reduce to about 5% at about 25 aperture radii downstream for the 0° case, but within 9 aperture radii for the remaining angles. This figure demonstrates that the far-field equation will typically produce accurate results within nine aperture radii downstream of a NEXT accelerator grid aperture.

B. Downstream Neutral Density from the Ion Thruster Grids Only

For this section, only the discharge chamber neutral loss through the grids is modeled. The contributions of the neutralizer and background vacuum facility neutrals are neglected so that near- and far-field comparisons can be made. The effect of the upstream screen grid was included (i.e., $F_{\text{scrn}} = 0.93$). In addition, the neutral density within the discharge chamber was assumed to be constant, so that $D(\gamma, \beta) = 1$ in Eq. (14). This constant neutral density assumption is an oversimplification because past studies have shown the upstream neutral density to be lower in center of the chamber due to neutral depletion from ionization [37,38]. Unfortunately, the neutral density distribution in a NEXT discharge chamber has not yet been measured. The neutral temperature was also assumed to be the same as the discharge chamber wall and temperatures. Although the neutrals escaping the discharge cathode will be much hotter, their impact is negligible because only an estimated 1% of the total neutral loss rate is composed of cathode hot neutrals that enter the grid apertures without first being reflected from a thruster surface.

The nondimensional neutral density downstream of a NEXT ion thruster from neutrals escaping through the grid apertures is shown in Fig. 11. This was determined using Eq. (16), which includes the rigorous calculation of Eq. (10) for the downstream neutral density from a single aperture. As the figure illustrates, the neutral density drops rapidly from the ion thruster grids into the downstream region due to the rapid expansion of the neutrals as they exit the accelerator apertures.

Close to the thruster grids, the contribution of adjacent apertures to the downstream neutral density of any given aperture can be examined. The neutral density downstream of the center aperture of a NEXT accelerator grid (i.e., $r = 0$) from Eq. (16) and the adjacent webbing (i.e., $r = l_{\text{cc}}/2$) is compared in Fig. 12 to that from a single aperture from Eq. (10). The number densities at $r = 0$ and $r = l_{\text{cc}}/2$ converge within three aperture radii for the multiple aperture case and within six radii for the single aperture case. More important, however, are the downstream magnitudes. The multiple apertures of the grids increase the downstream neutral density of the center aperture by a factor of 10 compared with that of the single aperture at only about 6.5 aperture radii from the accelerator grid. This demonstrates the significant contribution of adjacent apertures to the downstream neutral density of any given aperture for the NEXT ion thruster grids.

Although Eq. (10) represents a rigorous solution for downstream neutral density of a single aperture, its use in Eq. (16) can be cumbersome and computationally costly. However, the far-field assumptions used for solving the downstream neutral density of a perforated grid in Eqs. (13) and (15) are significantly less cumbersome to use and can be computed more quickly. So, it would be of value to determine how accurate Eqs. (13) and (15) are close to a NEXT ion thruster. Figure 13 compares the results of Eqs. (13) and (15) to Eq. (16) along the centerline of the grids and at a radius of $l_{\text{cc}}/2$ (i.e., between two apertures). As the figure illustrates, the far-field results converge rapidly onto the more rigorous results of Eq. (16). In fact, differences reduce to 1% within about five accelerator aperture radii from the accelerator grid. Because the NEXT accelerator aperture diameter is so small in comparison to the overall grid size, the far-field assumptions used in Eqs. (13) and (15) produce accurate neutral densities within about 3 mm of the NEXT thruster's accelerator grid.

Figure 13 also demonstrates another simplifying assumption that can be employed for the NEXT grids. Equation (15) neglects the contribution of individual apertures by treating the entire domed grid surface as a neutral-emitting surface whose angular distribution is corrected for the beaming effects of the cylindrical apertures. Because differences between the densities of Eqs. (15) and (16) decrease to 1% within about five accelerator aperture radii from the

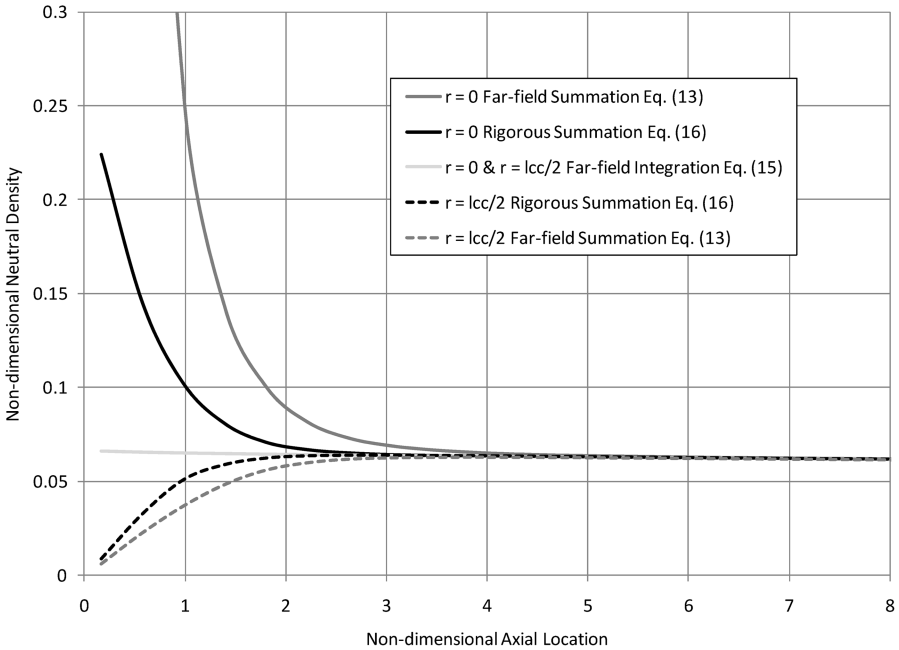

Fig. 13 Nondimensional downstream neutral density from a NEXT ion thruster along the grid centerline and at $r = l_{\text{cc}}/2$ using equations Eqs. (13), (15), and (16).

accelerator grid, such a simplifying assumption also produces accurate neutral densities within about 3 mm of the NEXT thruster's accelerator grid. Because of the ease of using this equation and the accuracy of the results, Eq. (15) will be used for the remainder of this study.

C. Total Downstream Neutral Density

The contributions of the neutralizer and background vacuum facility neutrals are included in this section. For all of the following calculations, a NEXT ion thruster geometry was assumed. In addition, the neutral density within the discharge chamber was assumed to be constant so that $D(\gamma, \beta) = 1$ in Eq. (14), and the effect of the upstream screen grid was included (i.e., $F_{\text{scrn}} = 0.93$).

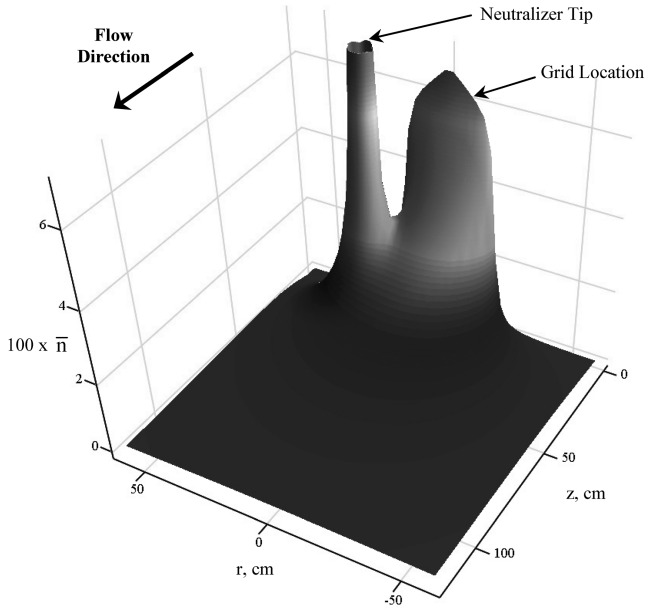

Fig. 14 Nondimensional neutral density downstream of a NEXT ion thruster operating at full power in space. The neutral density within the discharge chamber was assumed constant and the neutral loss rate from the neutralizer was 2.8 sccm.

The effect of neutrals from the neutralizer on the downstream neutral density for an NEXT ion thruster operating at full power is shown in Fig. 14, which excludes the effect of background vacuum facility neutrals and therefore represents operation in space. For a NEXT thruster operating at full power, the neutral loss rates are estimated to be 7.05 sccm for the discharge chamber and 2.8 sccm for the neutralizer. The discharge chamber neutral temperature was assumed to be 300°C while the neutralizer neutral temperature was assumed to be 1100°C [35]. The figure illustrates the impact of the neutralizer neutrals on the downstream neutral density. The high neutral density surrounding the neutralizer was due to neutrals being distributed across such a small keeper orifice area compared with that of the grid area. Figure 15 plots the nondimensional neutral density as a function of axial location with and without neutralizer neutrals at radial locations of 18 cm near and opposite the neutralizer (i.e., $\beta = 0$ and 180°, respectively). The 18 cm radial location was selected because it is the edge of the perforate grid radius. As expected, the neutralizer does not contribute to the density upstream of the neutralizer tip because there is no direct line of sight there. However, beyond that, the density increases by as much as 68% close to the neutralizer. Further downstream, the neutralizer's off-center effect is minimized, but the density is still about 22% larger because of the neutralizer's contribution.

The effect of background neutrals from the vacuum facility on the downstream neutral density for an NEXT ion thruster operating at full power is shown in Fig. 16. Here, the background pressure was set to 6.7×10^{-4} Pa (5×10^{-6} torr) with a background neutral temperature of 20°C. The effect of neutralizer neutrals was included in this figure using the same assumptions as for Fig. 14. The figure illustrates the significant impact of the facility neutrals on the neutral density, especially in the far field. To more clearly illustrate this effect, Fig. 15 shows the effect of vacuum facility neutrals on the nondimensional neutral density as a function of axial location at radial locations of 18 cm near and opposite the neutralizer. Although the contributions of the grid and neutralizer are significant close to them, the vacuum facility contribution represents the vast majority of the neutral density further away.

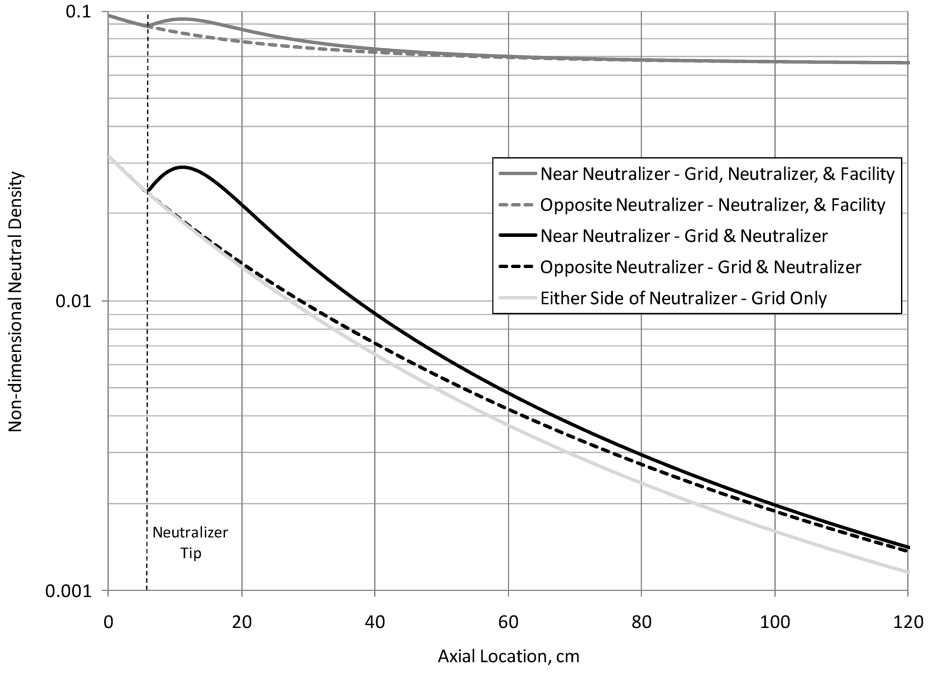

Fig. 15 Nondimensional neutral density downstream of a NEXT ion thruster operating at full power with and without neutralizer and vacuum facility contributions. The two radial locations shown include $r = 18$ cm in the direction of the neutralizer (i.e., $\beta = 0°$) and $r = 18$ cm opposite the neutralizer (i.e., $\beta = 180°$). The neutralizer tip is located at about $z = 6$ cm.

D. Model Verification

The neutral density model was verified by checking conservation of mass between the thruster (i.e., grid and neutralizer exit planes) and various downstream axial locations. To do this, the downstream flux of neutrals had to be determined. The fundamental equation for this flux is given by [39]

$$\Gamma = \frac{c}{4 \cdot \pi} \cdot \int_{A_o} n_o \cdot \frac{\cos(\alpha) \cdot \cos(\delta)}{L^2} \cdot \mathrm{d}A_o \tag{25}$$

This equation is similar to the neutral density equation (i.e., Eq. (3)), except for the inclusion of the mean thermal speed of the neutrals, c, and the cosine of the angle between the downstream surface normal and the line connecting the emission and collection sites, δ, which is shown in Figs. 6 and 7. Equation (25) was used to derive the grid and neutralizer neutral downstream fluxes in a manner similar to the downstream neutral density derivations of Eqs. (15) and (21), and the results were summed to determine a thruster neutral flux. The resulting thruster flux was integrated radially at several downstream axial locations to determine a thruster neutral loss rate. These downstream neutral loss rates were compared with the discharge chamber and neutralizer neutral loss rates to ensure mass conservation. Numerous downstream locations were examined from 1 cm to 100 m, and in all cases, mass was conserved.

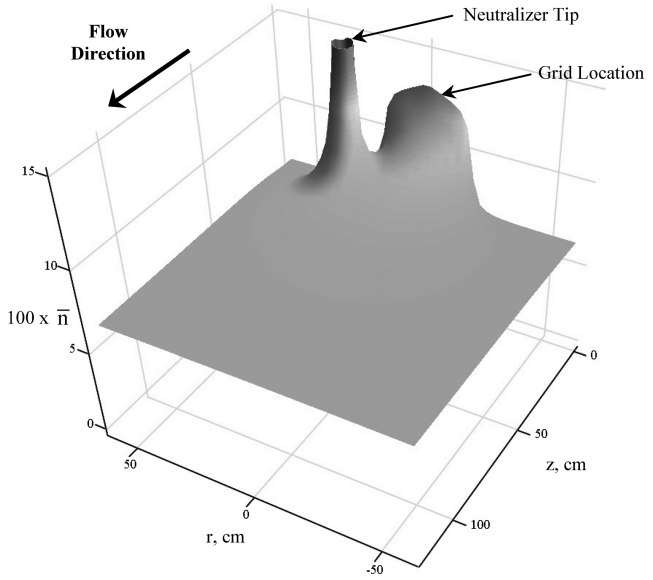

Fig. 16 Nondimensional neutral density downstream of a NEXT ion thruster operating at full power with vacuum facility neutrals. The neutral density within the discharge chamber was assumed constant and the neutral loss rate from the neutralizer was 2.8 sccm. Vacuum facility background pressure was set to 6.7×10^{-4} Pa (5×10^{-6} torr).

E. Assessment of Past Assumptions

This section will assess some past simplifying assumptions that were made to more easily determine the downstream neutral density. These simplifying assumptions included neglecting the effect of neutralizer neutrals, neglecting the beaming effect of the cylindrical aperture walls, and assuming a flat grid. All of these assumptions will be examined with a NEXT ion thruster operating at full power.

The impact of the neutralizer was already assessed in the prior section (see Fig. 15). Neglecting the neutralizer's contribution to the downstream neutral density would lead to a neutral density that is 22% lower than actual in the far field for a NEXT thruster operating at full power. The impact of neglecting the beaming effect of the aperture walls is illustrated in Fig. 17 along the grid centerline. In this figure, the effects of neutralizer and vacuum facility background neutrals were ignored to facilitate direct comparisons. And although neutrals were assumed to exit an aperture diffusely, the upstream neutral density was set equal to that where the beaming effect is included (i.e., the baseline case). The figure shows that the neutral density begins higher than the baseline case close to the grids because the diffuse angular distribution contributes more neutrals to the grid centerline close to the grid. But further away, this same effect leads to lower neutral densities as the neutrals expand more rapidly. So, ignoring the beaming effect of the aperture walls leads to an overestimation of 14% close to the grid and an underestimation that approaches 30% in the far field.

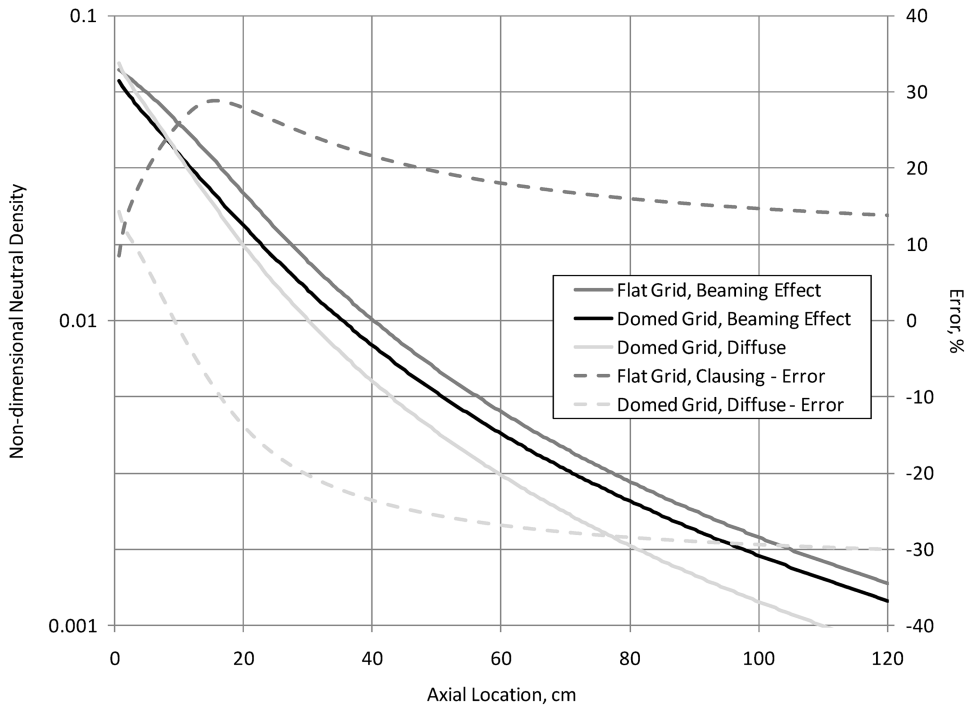

Fig. 17 Nondimensional downstream neutral density and errors as a function of axial location along the grid centerline for: a domed NEXT grid that includes the beaming effect of the aperture walls; a domed NEXT grid that excludes the beaming effect of the aperture walls (diffuse assumption); and a flat grid that includes the beaming effect of the aperture walls.

The impact of assuming a flat grid is also illustrated in Fig. 17 along the grid centerline. The upstream neutral density was set equal to that of the domed grid case, and the beaming effect of the aperture walls is included. The figure shows that the neutral density is always higher than the baseline case because the flat grid collimates the outgoing neutrals. The flat grid assumption led to neutral density overestimations along the grid centerline of as large as 29% in the near field and 14% in the far field. These results demonstrate the significance of grid shape, the beaming effect of the aperture walls, and the neutralizer neutral loss rate on the downstream neutral density.

V. Conclusions

The details of a model for determining the neutral density downstream of a gridded ion thruster were presented. A rigorous examination of the possible sources of neutrals emanating from and surrounding a NEXT ion thruster concluded that the most significant contributors to the downstream neutral density included discharge chamber neutrals escaping through the perforated grids, neutrals escaping from the neutralizer, and vacuum facility background neutrals. Because ion thrusters typically operate in the free molecular flow regime, each neutral density source was modeled separately and the results added together to determine the total neutral density.

For the neutral flux through the grids, near- and far-field equations were presented for rigorously determining the neutral density downstream of a cylindrical aperture. These equations included the beaming effect of the aperture walls. These equations were subsequently integrated into a spherically-domed convex grid geometry with a hexagonal array of apertures for determining neutral densities downstream of the ion thruster grids. The neutrals escaping from an off-center neutralizer were also modeled assuming diffuse neutral emission from the neutralizer keeper orifice. Finally, the effect of the surrounding vacuum facility neutrals was included and assumed to be uniform.

The model was then used to predict the neutral density downstream of a NEXT ion thruster with and without neutralizer flow and a vacuum facility background pressure. Individual aperture results showed that far-field equation errors reduced to about 5% within nine aperture radii, indicating that the far-field equation will produce accurate results close to a NEXT accelerator grid aperture. Because the NEXT accelerator aperture diameter is so small in comparison to the overall grid size, the far-field equations were shown to produce accurate neutral densities within about 3 mm of the NEXT thruster's accelerator grid. This was significant because these equations are far less cumbersome to use than the more rigorous equations and are computationally efficient.

The impacts of the neutralizer neutral loss rate and the surrounding vacuum facility neutrals were separately assessed for a NEXT ion thruster operating at full power. Beyond the neutralizer exit plane, the density increased by as much as 68% at a radial location of 18 cm close to the neutralizer. Further downstream, the neutralizer's off-center effect was minimized, but the density was still about 22% larger because of the neutralizer's contribution. Vacuum facility effects were assessed at a background pressure set to 6.7×10^{-4} Pa (5×10^{-6} torr). Although the contributions of the grid and neutralizer were still significant close to them, the vacuum facility contribution represented the vast majority of the neutral density further away. Proper modeling of charge-exchange production in the ion beam requires incorporating the effects of neutralizer neutral efflux and vacuum facility neutrals.

The impact of past simplifying assumptions for predicting downstream neutral densities were also assessed for a NEXT ion thruster. Neglecting the beaming effect of the aperture walls along the grid centerline led to an overestimation of neutral density by 14% close to the grid and an underestimation that approached 30% in the far field. Assuming a flat grid led to neutral density overestimations along the grid centerline of as large as 29% in the near field and 14% in the far field. These results demonstrated the significance of grid shape, the beaming effect of the aperture walls, and the neutralizer neutral loss rate on the downstream neutral density.

References

[1] Rawlin, V. K., Sovey, J. S., Hamley, J. A., Bond, T. A., Matranga, M., and Stocky, J. F., "An Ion Propulsion System for NASA's Deep Space Missions," AIAA Paper 99-4612, Sept. 1999.

[2] Polk, J. E., Brinza, D., Kakuda, R. Y., Brophy, J. R., Katz, I., Anderson, J. R., Rawlin, V. K., Patterson, M. J., Sovey, J., and Hamley, J., "Demonstration of the NSTAR Ion Propulsion System on the Deep Space One Mission," International Electric Propulsion Conference Paper 2001-075, Oct. 2001.

[3] Brophy, J. R., Brinza, D., Polk, J. E., and Henry, M., "The DS1 Hyper-Extended Mission," AIAA Paper 2002-3673, July 2002.

[4] Brophy, J. R., Marcucci, M. G., Ganapath, G. B., Gates, J., Garner, C. E., Klatte, M., Lo, J., Nakazono, B., and Pixler, G., "Implementation of the Dawn Ion Propulsion System," AIAA Paper 2005-4071, July 2005.

[5] Brophy, J. R., Garner, C. E., and Mikes, S., "Dawn Ion Propulsion System: Initial Checkout After Launch," *Journal of Propulsion and Power*, Vol. 25, No. 6, Nov.–Dec. 2009, pp. 1189–1202. doi:10.2514/1.40480

[6] Patterson, M. J., and Benson, S. W., "NEXT Ion Propulsion System Development Status and Performance," AIAA Paper 2007-5199, July 2007.

[7] Benson, S. W., and Patterson, M. J., "NEXT Ion Propulsion System Progress Towards Technology Readiness," AIAA Paper 2008-5285, July 2008.

[8] Pollard, J. E., Diamant, K. D., Crofton, M. W., Patterson, M. J., and Soulas, G. C., "Spatially-Resolved Beam Current and Charge-State Distributions for the NEXT Ion Engine," AIAA Paper 2010-6779, July 2010.

[9] Miller, J. S., Pullins, S. H., Levandier, D. J., Chiu, Y., and Dressler, R. A., "Xenon Charge Exchange Cross Sections for Electrostatic Thruster Models," *Journal of Applied Physics*, Vol. 91, No. 3, 2002, pp. 984–991. doi:10.1063/1.1426246

[10] Clausing, P., "The Formation of Beams in Molecular Streaming," *Z. Physik*, Vol. 66, 1930, pp. 471–476.

[11] Dayton, B. B., "Gas Flow Patterns at Entrance and Exit of Cylindrical Tubes," *National Symposium on Vacuum Technology Transactions*, Pergamon, New York, 1956, pp. 5–11.

[12] Reynolds, T. W., and Richley, E. A., "Distribution of Neutral Propellant from Electric Thrusters onto Spacecraft Components," NASA TN D-5576, Dec. 1969.

[13] Hall, D. F., Newnam, B. E., and Womack, J. R., "Electrostatic Rocket Exhaust Effects on Solar-Electric Spacecraft Subsystems," AIAA Paper 1969-271, March 1969.

[14] Samanta Roy, R. I., Hastings, D. E., Gatsonis, N. A., and Mauk, B. H., "A Hybrid Particle-in-Cell/Fluid Model of Ion Thruster Plumes," AIAA Paper 1994-0421, Jan. 1994.

[15] Samanta Roy, R. I., Hastings, D. E., and Gatsonis, N. A., "Ion Thruster Plume Modeling for Backflow Contamination," *Journal of Spacecraft and Rockets*, Vol. 33, No. 4, July–Aug. 1996, pp. 525–534. doi:10.2514/3.26795

[16] Samanta Roy, R. I., and Hastings, D. E., "Three-Dimensional Modeling of Dual Ion-Thruster Plumes for Spacecraft Contamination," *Journal of Spacecraft and Rockets*, Vol. 33, No. 4, July–Aug. 1996, pp. 519–524. doi:10.2514/3.26794

[17] Samanta Roy, R. I., Hastings, D. E., and Gatsonis, N. A., "Numerical Study of Spacecraft Contamination and Interactions by Ion-Thruster Effluents," *Journal of Spacecraft and Rockets*, Vol. 33, No. 4, July–Aug. 1996, pp. 535–542. doi:10.2514/3.26796

[18] Wang, J., Brinza, D., Goldstein, R., Polk, J., Henry, M., Young, D. T., Hanley, J. J., Nordholt, J., Lawrence, D., and Shappirio, M., "Deep Space One Investigations of Ion Propulsion Plasma Interactions: Overview and Initial Results," AIAA Paper 1999-2971, June 1999.

[19] Wang, J., Brinza, D., and Young, M., "Modeling of Ion Propulsion Plasma Environment for Deep Space 1," AIAA Paper 2000-3528, July 2000.

[20] Wang, J., Cao, Y., and Kafafy, R., "Electric Propulsion Plume Modeling Using Parallel Supercomputers," AIAA Paper 2006-3559, June 2006.

[21] Cho, M., Saionji, A., Toyoda, K., Nozaki, Y., and Sato, T., "Interaction Between High Voltage Solar Array and Ion Thruster Plasma," International Electric Propulsion Conference Paper 2003-053, March 2003.

[22] Davis, V. A., Katz, I., Mandell, M. J., Brinza, D. E., Henry, M. D., Wang, J. J., and Young, D. T., "Ion Engine Generated Charge Exchange Environment: Comparison Between NSTAR Flight Data and Numerical Simulations," AIAA Paper 2000-3529, July 2000.

[23] Boyd, I. D., VanGilder, D. B., and Liut, X., "Monte Carlo Simulation of Neutral Xenon Flows in Electric Propulsion Devices," *Journal of Propulsion and Power*, Vol. 14, No. 6, Nov.–Dec. 1998, pp. 1009–1015.
doi:10.2514/2.5366

[24] VanGilder, D. B., Font, G. I., and Boyd, I. D., "Hybrid Monte Carlo Particle-in-Cell Simulation of an Ion Thruster Plume," *Journal of Propulsion and Power*, Vol. 15, No. 4, Aug. 1999, pp. 530–538.
doi:10.2514/2.5475

[25] Nishida, M., Hyakutake, T., Kuninaka, H., and Toki, K., "DCMC-PIC Analysis of a Plume from a Small Ion Engine," International Electric Propulsion Conference Paper 2001-110, Oct. 2001.

[26] Fergason, S. D., "Ion Thruster Plume Simulation Using Clustered PC Workstations," AIAA Paper 2005-966, Jan. 2005.

[27] Kameyama, I., Monheiser, J. M., and Wilbur, P. J., "A Numerical Model of Thruster-Exhaust Plumes," International Electric Propulsion Conference Paper 1997-180, Aug. 1997.

[28] Mandell, M. J., Davis, V. A., Pencil, E. J., Patterson, M. J., McEwen, H. K., Foster, J. E., and Snyder, J. S., "Modeling the NEXT Multithruster Array Test With Nascap-2k," *IEEE Transactions on Plasma Science*, Vol. 36, No. 5, 2008, pp. 2309–2318.
doi:10.1109/TPS.2008.2003534

[29] Kuharski, R. A., Mandell, M. J., Gardner, B. M., Katz, I., and Vaughan, D., "Ion Engine Neutralizer Erosion in Lab and Space," AIAA Paper 2005-3880, July 2005.

[30] Soulas, G. C., "Gas Flux and Density Surrounding a Cylindrical Aperture in the Free Molecular Flow Regime," NASA TM 2011-216970, March 2011 (to be published).

[31] Soulas, G. C., Patterson, M. J., Pinero, L., Herman, D. A., and Snyder, J. S., "NEXT Single String Integration Test Results," AIAA Paper 2009-4816, Aug. 2009.

[32] Soulas, G. C., "Modeling Neutral Densities Downstream of a Gridded Ion Thruster," AIAA Paper 2010-6699, July 2010.

[33] Mikellidis, I. G., Goebel, D. M., Snyder, J. S., Katz, I., and Herman, D. A., "Neutralizer Hollow Cathode Simulations and Validations with Experiments," AIAA Paper 2009-5196, Aug. 2009.

[34] Gombosi, T. I., *Gas Kinetic Theory*, Cambridge Univ. Press, Cambridge, England, U.K., 1994, pp. 18–35.

[35] Van Noord, J. L., "NEXT Ion Thruster Thermal Model," AIAA Paper 2007-5218, July 2007.

[36] Wilbur, P. J., and Brophy, J. R., "The Effect of Chamber Wall Temperature on Ion Thruster Performance," International Electric Propulsion Conference Paper 84-67, May 1984.

[37] Sengupta, Goebel, D., Fitzgerald, D., Owens, A., Tynan, G., and Doerner, R., "Experimentally Determined Neutral Density and Plasma Parameters in a 30 cm Ion Engine," AIAA Paper 2004-3613, July 2004.

[38] Wirz, R., and Katz, I., "A Preliminary 2-D Computational Model of an Ion Thruster Discharge Chamber," AIAA Paper 2003-5163, July 2003.

[39] Richley, E. A., and Bogart, C. D., "Numerical Solutions of Knudsen Flow Entering a Circular Tube Through a Small Axial Orifice," NASA TN D-2115, June 1964.

L. King
Associate Editor